General Disclaimer

One or more of the Following Statements may affect this Document

- This document has been reproduced from the best copy furnished by the organizational source. It is being released in the interest of making available as much information as possible.

- This document may contain data, which exceeds the sheet parameters. It was furnished in this condition by the organizational source and is the best copy available.

- This document may contain tone-on-tone or color graphs, charts and/or pictures, which have been reproduced in black and white.

- This document is paginated as submitted by the original source.

- Portions of this document are not fully legible due to the historical nature of some of the material. However, it is the best reproduction available from the original submission.

Produced by the NASA Center for Aerospace Information (CASI)

AD-A022 241

90 GHz RADIOMETRIC IMAGING

H. E. King, et al

Aerospace Corporation

Prepared for:

Space and Missile Systems Organization

19 February 1976

90 GHz RADIOMETRIC IMAGING

H. E. KING, J. D. WHITE, W. J. WILSON, and T. T. MORI
Electronics Research Laboratory
Laboratory Operations
The Aerospace Corporation
El Segundo, Calif. 90245

J. P. HOLLINGER, B. E. TROY, and J. E. KENNEY
Space Sciences Division
Naval Research Laboratory
Washington, D. C. 20090

and

J. T. McGOOGAN
Applied Sciences Directorate
Wallops Island, Va. 23337

19 February 1976

Final Report

Prepared for

This report was submitted by The Aerospace Corporation, El Segundo, CA 90245, under Contract F04701-75-C-0076 with the Space and Missile Systems Organization, Deputy for Advanced Space Programs, P. O. Box 92960, Worldway Postal Center, Los Angeles, CA 90009. It was reviewed and approved for The Aerospace Corporation by A. H. Silver, Director, Electronics Research Laboratory. Lt. Ronald C. Lawson, SAMSO/DYN, was the project officer.
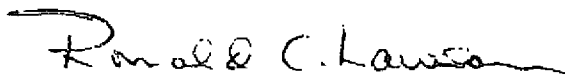
This report has been reviewed by the Information Office (OI) and is releasable to the National Technical Information Service (NTIS). At NTIS, it will be available to the general public, including foreign nations.

This technical report has been reviewed and is approved for publication. Publication of this report does not constitute Air Force approval of the report's findings or conclusions. It is published only for the exchange and stimulation of ideas.

FOR THE COMMANDER

Ronald C. Lawson
1st Lt., U.S. Air Force
Office of Research Applications
Deputy for Technology

SECURITY CLASSIFICATION OF THIS PAGE *(When Data Entered)*

REPORT DOCUMENTATION PAGE		READ INSTRUCTIONS BEFORE COMPLETING FORM
1. REPORT NUMBER SAMSO-TR-76-37	2. GOVT ACCESSION NO.	3. RECIPIENT'S CATALOG NUMBER
4. TITLE *(and Subtitle)* 90 GHz RADIOMETRIC IMAGING		5. TYPE OF REPORT & PERIOD COVERED Final
		6. PERFORMING ORG. REPORT NUMBER TR-0076(6230-40)-1
7. AUTHOR(s) H. E. King, J. D. White, W. J. Wilson, T. T. Mori, J. P. Hollinge , B. E. Troy, J. E. Kenney, and J. T. McGoogan		8. CONTRACT OR GRANT NUMBER(s) F04701-75-C-0076
9. PERFORMING ORGANIZATION NAME AND ADDRESS The Aerospace Corporation El Segundo, Calif. 90245		10. PROGRAM ELEMENT, PROJECT, TASK AREA & WORK UNIT NUMBERS
11. CONTROLLING OFFICE NAME AND ADDRESS Space and Missile Systems Organization Air Force Systems Command Los Angeles, Calif. 90009		12. REPORT DATE 19 February 1976
		13. NUMBER OF PAGES 49 53
14. MONITORING AGENCY NAME & ADDRESS*(If different from Controlling Office)*		15. SECURITY CLASS. *(of this report)* Unclassified
		15a. DECLASSIFICATION/DOWNGRADING SCHEDULE

16. DISTRIBUTION STATEMENT *(of this Report)*

Approved for public release; distribution unlimited.

17. DISTRIBUTION STATEMENT *(of the abstract entered in Block 20, if different from Report)*

18. SUPPLEMENTARY NOTES

19. KEY WORDS *(Continue on reverse side if necessary and identify by block number)*

Passive Remote Earth Sensing
Millimeter Wave Radiometric Imaging
90 GHz Radiometer

20. ABSTRACT *(Continue on reverse side if necessary and identify by block number)*

A 90-GHz (3 mm wavelength) radiometer with a noise output fluctuation of 0.22°K (RMS), with a scanning antenna beam mirror, and the data processing system are described. Real-time radiometric imaging of terrain and man-made objects are shown. Flying at an altitude of 1500 ft a radiometer antenna with a 2° halfpower beamwidth can distinguish landforms, waterways, roads, runways, bridges, ships at sea and their wakes, aircraft on runways, and athletic fields. A flight taken at an altitude of 3000 ft with approximately 2000 ft of clouds below the radiometer demonstrates the

DD FORM 1473
(FACSIMILE)

19. KEY WORDS (Continued)

20. ABSTRACT (Continued)

ability to distinguish bridges, rivers, marshland and other landforms even though the clouds are optically opaque. The radiometric images of a few representative scenes along with photographs of the corresponding scenes are presented to demonstrate the resolution of the imager system. Antenna temperature distributions of a variety of land targets are tabulated and the complexity of deriving target brightness temperatures from the measured antenna temperatures are discussed. Applications of millimeter wave radiometric images for civil and military systems are described.

PREFACE

The information in this Technical Report represents the results of a joint effort by the Naval Research Laboratory, NASA Wallops and The Aerospace Corporation. The authors wish to acknowledge G. G. Berry and H. B. Dyson, Electronics Research Laboratory of The Aerospace Corporation, for the development and evaluation of the radiometer; R. B. Dybdal, Electronics Research Laboratory, for the review and comments of the manuscript; and Ted Welti and Roger Navarro, and the pilots, crew, and staff at NASA-Wallops Flight Center for the flight-test support.

CONTENTS

TABLE

Preceding page blank

FIGURES

I. INTRODUCTION

Radiometric sensing of the earth's surface and atmosphere has been reviewed by Tomiyasu (Ref. 1) and in a paper describing the NASA Shuttle Imaging Microwave System (SIMS) experiment in Ref. 2. The Air Force and NASA have been interested in utilizing these measurement techniques for a number of years to measure meteorological phenomena and for navigation and guidance applications. The breadth of applications and wealth of information provided by radiometry is due to the variation of the emission, absorption and reflection properties of matter with the observational frequency, polarization and incidence angle. Microwave radiometric sensing of the earth can provide day and night operation while visual and IR sensing is limited to daytime measurements. Also visual and IR sensing is limited to clear days, while microwave radiometry has almost an all-weather capability. Wrixon (Ref. 3) reports that millimeter wave transmission through clouds is only reduced by a few dB (typically 2 to 5 dB) at 90 GHz while the reduction is <0.3 dB at 16 GHz. Later measurements by Lo, Fannin and Straiton (Ref. 4) show that for comparable cloud conditions the attenuation values are near that of Wrixon's data. Lo, et al, lists the 95 GHz cloud attenuation ≤ 1 dB for 7 different cloud types; i.e., the increase in total atmospheric attenuation when a particular cloud type is present. Spatial resolution of microwave sensors is determined by the antenna beamwidth; i.e., high resolution can be achieved only by antennas with large sizes with respect to a wavelength. (In contrast, the resolution of optical and IR sensors will exceed that of microwave sensors.) The millimeter wave spectrum is chosen to achieve high spatial resolution with relatively small antenna sizes.

Passive microwave imagers have proven of great value for the remote sensing of the environment. Two Electrically Scanning Microwave Radiometers (ESMR) are presently in use aboard satellites: the 19.35 GHz ESMR on NIMBUS 5 (launched in 1972) and a 37 GHz unit on NIMBUS 6, launched June 1975 (Refs. 5 and 6). NIMBUS 6 also carries a Scanning Microwave Spectrometer (SCAMS) for producing images (Ref. 7). A Scanning Multiple Microwave Radiometer

(SMMR) with five frequencies from 690 MHz to 37 GHz is being developed for both the NIMBUS G and SEASAT satellites for launch in 1978 (Ref. 8). NASA is also planning the Shuttle Imaging Microwave System (SIMS) experiment with 11 frequencies from 610 MHz to 118 GHz.

The U.S. Air Force has conducted a feasibility study contract to formulate a Microwave Imaging Sensor Study (MISS) that will map out the earth and to establish weather formations of the world (Ref. 9). The emphasis in MISS was devoted to the lower millimeter wave frequencies. The Air Force is presently responsible for the U. S. Defense Meteorological Satellite Program (DMSP) to provide a scanning multi-frequency radiometer near the oxygen absorption band at 5 mm wavelength (60 GHz) to obtain atmospheric temperature profiles (Ref. 10). The DMSP will not be an imager.

The emphasis on the present and future microwave earth observations imaging experiments are devoted primarily to observing atmospheric and geophysical parameters from satellites with surface resolutions of 4 or 5 km (SIMS) to 40 km for NIMBUS G. The purpose of the 90 GHz radiometric imaging experiment described herein is to acquire high resolution images with the ability of detecting detailed earth surface characteristics and man-made objects.

In the pursuit of passive remote sensing in the millimeter wave spectrum, the Naval Research Laboratory (NRL) and The Aerospace Corporation have been engaged in research and experimentation with millimeter radiometers for a number of years (Refs. 11 to 19) for a wide range of geophysical, atmospheric and astronomical investigations. Airborne radiometric measurements were made at 19.3 and 31 or 69.8 GHz of controlled marine oil spills and it was found that remote determination of the thickness and volume of sea surface oil spills was possible (Ref. 12). A versatile passive microwave imaging system covering the frequencies of 14, 19, 22, 31 and 90 GHz has been developed by NRL and Aerospace (90 GHz radiometer) for the generation of high-resolution maps of geographical and man-made objects (Ref. 13). The 90 GHz radiometric imaging portion of the system is described

in this report. The measurements presented here are the first known high-quality 90 GHz <u>real-time images</u> of land, water and man-made objects made from an aircraft. Previous 94 GHz imaging experiments described by Chalfin and Ricketts (Ref. 20) were limited to a radiometer installed on a mountain and requiring an hour to scan a field-of-view of approximately $30^{\circ} \times 45^{\circ}$ subtending the valley. Post-measurements data processing formulated the images.

Naval Research Laboratory (NRL), NASA Wallops, and Aerospace participated in a joint effort to develop and flight test a 90 GHz radiometric imaging system to gather scientific knowledge in radiometry and to formulate radiometric information of land, sea, ships and other targets that will be useful for DoD missions in terminal guidance, reconnaissance and other tactical operations. The system was designed to be adaptable to changes in its operational frequency, polarization and angular resolution as described in Section II. The system has been flight tested aboard the NASA Wallops C-54 aircraft. Images have been made at 90 GHz with a 2° HPBW (halfpower beamwidth) antenna and the results are presented in Section III. Simultaneously, during one flight, non-scanning nadir-viewing radiometers at 14 and 19 GHz recorded the temperature profile of the terrain. The antenna temperatures of pertinent targets at 14, 19 and 90 GHz are tabulated in this report.[*] Appendix A illustrates the complexity in determining the brightness temperatures from the measured antenna temperatures. Applications of millimeter wave radiometry for civil and DoD missions are outlined in Section IV. The staff at NRL (Hollinger, Kenney and Troy, Ref. 13) have a complete description of the 90 GHz imaging system and the test results.

---

[*] A comparison of the brightness temperatures with past workers was not performed and it will be a subject of a future report.

II. EQUIPMENT AND DATA PROCESSING

The imaging system mounted in a NASA C-54 aircraft consists of an oscillating mirror, a 90 GHz radiometer with a 2° HPBW horn-lens antenna, and the data acquisition unit. These three units are self contained and may be operated and controlled separately, providing a versatile arrangement of antenna and radiometer combinations. This arrangement readily allows changes in radiometers (i.e., change frequency), antennas and polarization.

A.   EQUIPMENT

The radiometer imaging configuration is shown in Fig. 1. The antenna electrical axis and the rotational axis of the mirror are collinear and parallel to the direction of flight. The antenna beam is scanned by the mirror at a constant angular rate in a transverse direction, generating a sawtooth or zigzag raster over the ground with aircraft motion.

The mirror is elliptically shaped with a minor axis of 8 in. It is mounted at an angle of 45° to its rotational axis and projects the same circular spot size to the antenna beam at all scan angles. With this arrangement the output variations caused by spillover energy of the antenna past the mirror are minimized with scan angle. The antenna aperture is placed as close as it is physically possible to the scanning mirror (the upper flange is within an inch of the mirror) and with this configuration the antenna patterns with and without the plate are expected to be the same for all practical purposes (Ref. 13). The mirror drive was designed and built by John Hill at the Watkins-Johnson Company. The oscillating motion is accomplished by alternately connecting the mirror shaft to contrarotating drive shafts with a magnetic clutch. The contrarotating drives are obtained from a common motor driven shaft by using gear-to-gear coupling and pulley-to-pulley coupling for the two senses of rotation. Only the thin magnetic clutch plate, mirror shaft and mirror reverse direction, minimizing the inertia to be overcome by the drive. Since the drive power required is highest during the very short time when the rotation is reversed, a flywheel is used to store energy during the remainder of the cycle which results in minimal electric drive motor requirements. The mirror is scanned $\pm 32^\circ$ from nadir in 0.1 sec or 640 deg/sec and it reverses direction in < 1 msec.

FLIGHT
DIRECTION

OSCILLATING MIRROR

HATCH OPENING

MIRROR SCANS ±32° FROM NADIR
SCAN TIME = 0.1 sec
HPBW = 2°
$\Delta T = 2.78°K$ / RESOLUTION CELL
ALTITUDE = 1500 ft
SPEED=173mph, 254 fps

RADIOMETER
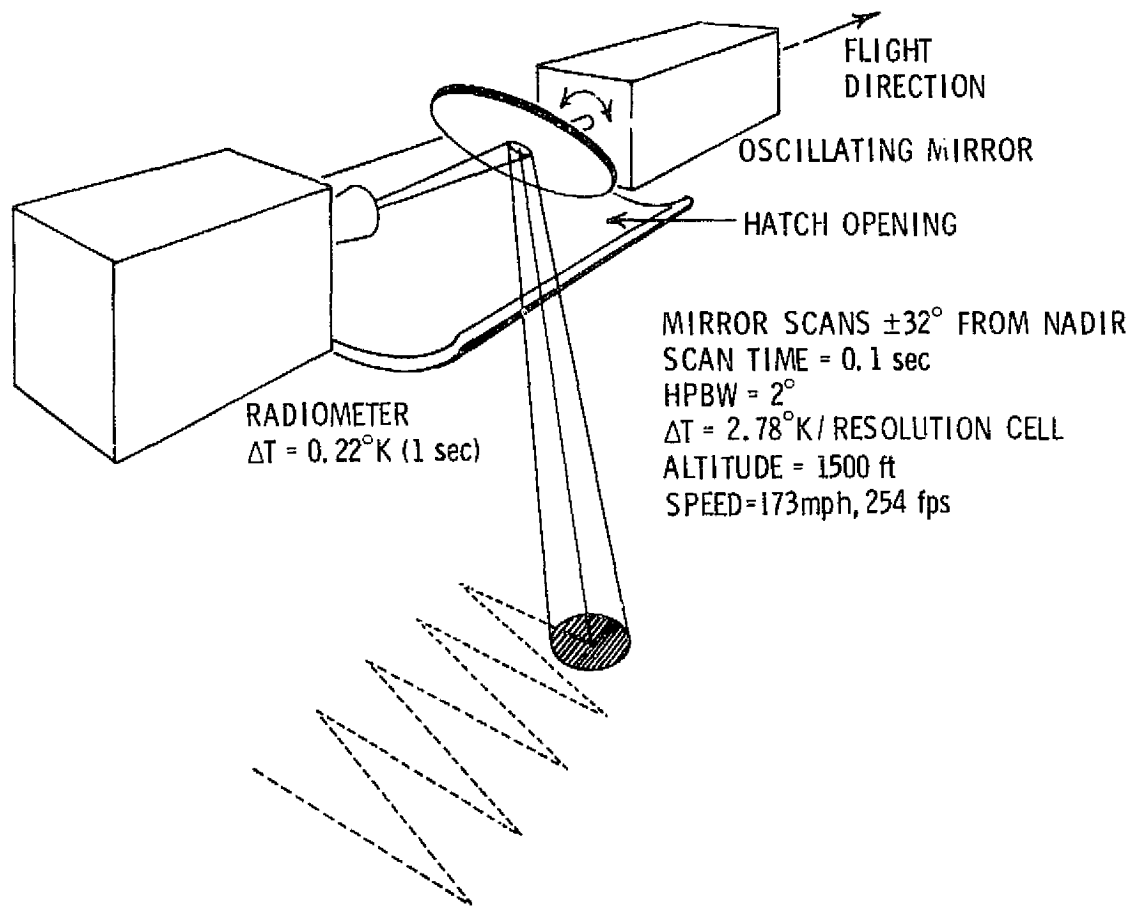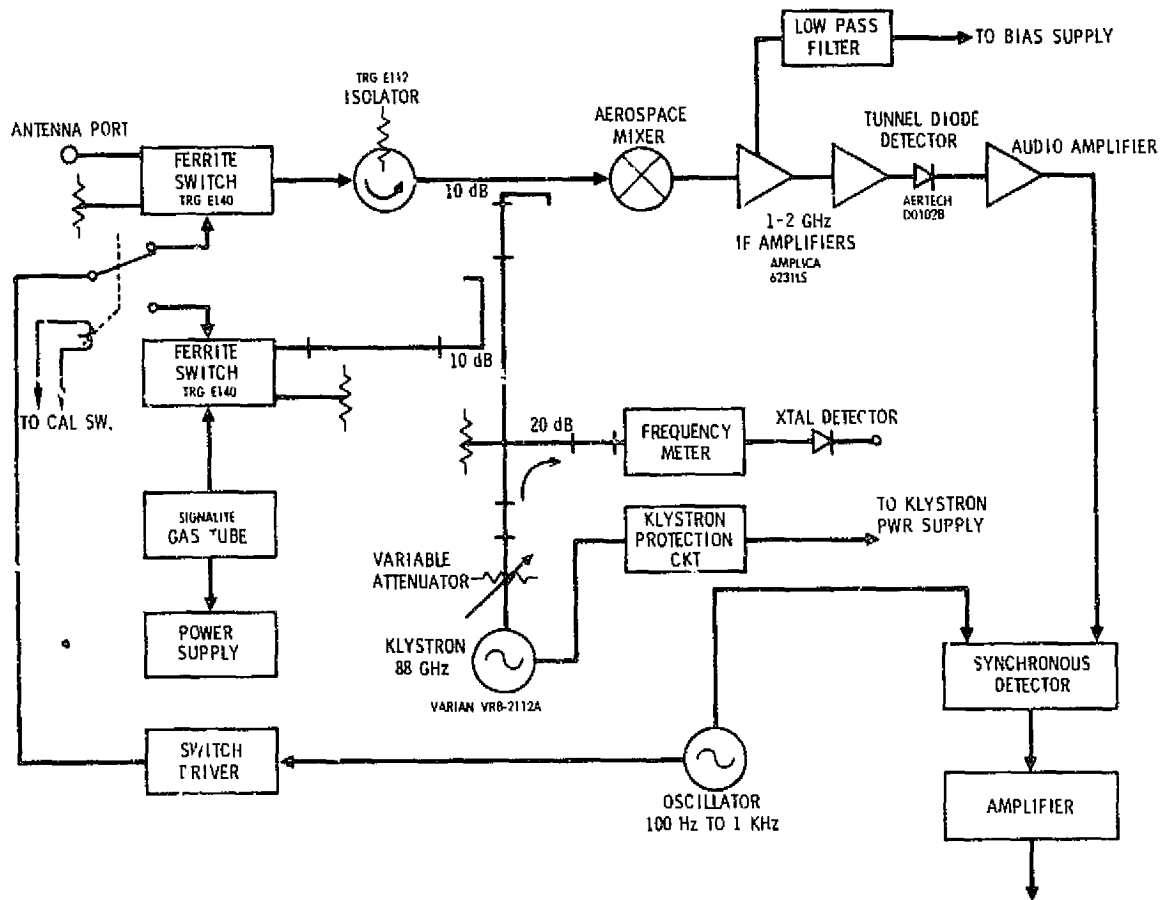$\Delta T = 0.22°K$ (1 sec)

Fig. 1.   90 GHz Radiometric Imager Configuration and Characteristics

The block diagram of the 90 GHz radiometer electronics is given in Fig. 2. It is a conventional Dicke radiometer using a ferrite switch for the synchronous load switching. The mixer was developed at Aerospace Corporation and is shown in Fig. 3 (Ref. 21). The mixer consists of a GaAs Schottky barrier diode (2.5μ diam contacts) mounted in full height WR-12 waveguide. IF matching transformers were not used to match the diode impedance. The IF VSWR is < 1.5:1 at an IF frequency of 3 GHz. The mixer has a single sideband conversion loss of < 8 dB with an IF bandwidth output of 1 to 2 GHz. The IF transistor preamplifiers have a noise figure < 3 dB over the 1 to 2 GHz band. The LO power is coupled into the mixer using a 10 dB directional coupler. An isolator is used to prevent the modulation of the LO power which is reflected from the mixer toward the antenna port (Ref. 14). The ferrite devices typically have a 1 to 1.5 dB insertion loss. With the RF components arranged as in Fig. 2 the measured noise output fluctuation (ΔT) is 0.22°K for a one second integration time. Four views of the radiometer package are shown in Fig. 4. The TRG scalar horn antenna with lens correction is located at one end of the radiometer housing. The major components are identified on the various photographs.

B.   DATA PROCESSING

The surface resolution is generally defined as the projection of the antenna HPBW on the surface. To completely specify the observed brightness temperature distribution, the scene to be imaged should be sampled at least as close as one-half the surface resolution or one-half the HPBW. Thus, the radiometer data is collected at intervals of 1° along the scan line (i.e., one-half the HPBW of 2°). Similarly, the surface resolution obtainable is twice the distance the aircraft moves forward in the time required to complete one scan or 0.1 sec. For these tests, the aircraft speed of 150 kt or 254 fps, the resolution is approximately 50 ft and does not depend directly upon the beamwidth. Practically, however, the resolution achievable depends upon the system sensitivity. Surface features with sufficient contrast may be resolved even if the targets are smaller than the resolution cell, as will be illustrated later for an athletic field and bridges.

Fig. 2.   Block Diagram of 90 GHz Radiometer

(a)   Photograph

I.F. BROADBAND OUTPUT

DUMBBELL SHORT WITH TEFLON BUSHINGS

RF CHOKE

DIODE

RF IN

10

5

SET SCREW

DIODE POST

MICROMETER MOVEMENT

(b)   Cross-sectional View
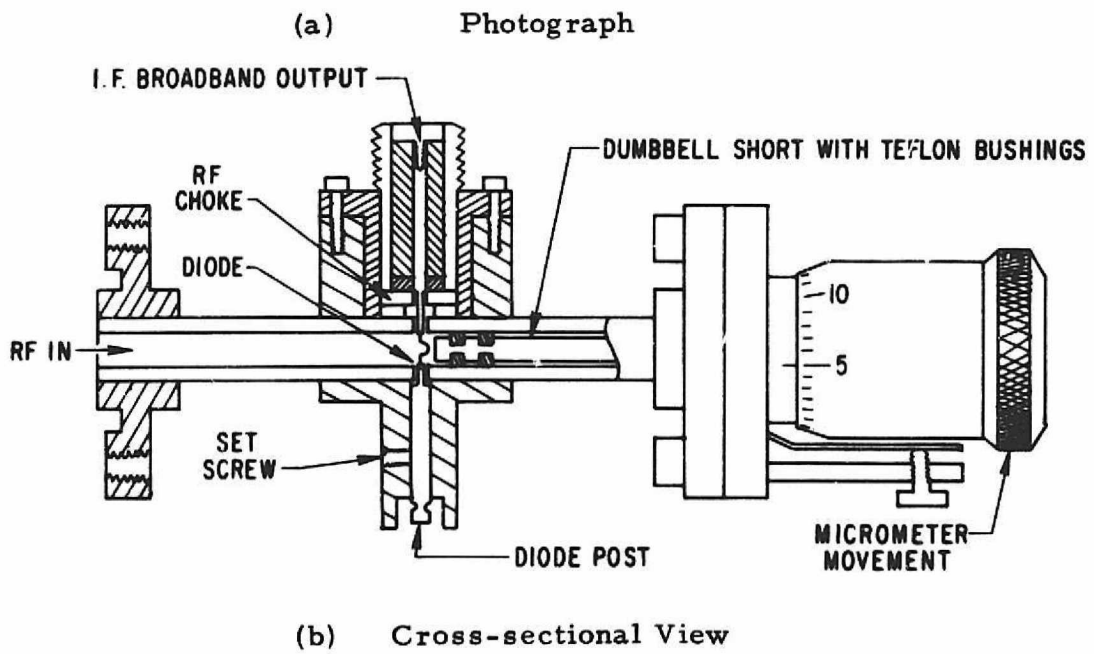
Fig. 3.   90 GHz Mixer

(a)   Radiometer and Control Panel

Fig. 4.   Photographic Views of Radiometer

(b)   Side View Showing Calibration and LO Components

Fig. 4 (continued)

(c)   Top View Showing RF and IF Components

Fig. 4 (continued)

(d)   Side View Showing IF and Audio Circuits

Fig. 4   (Concluded)

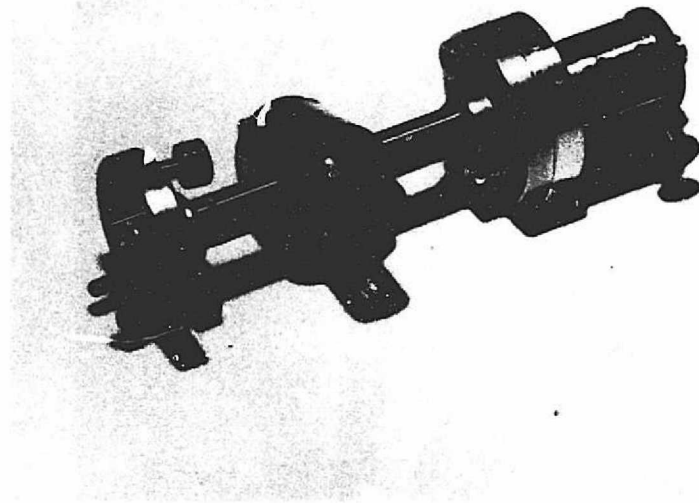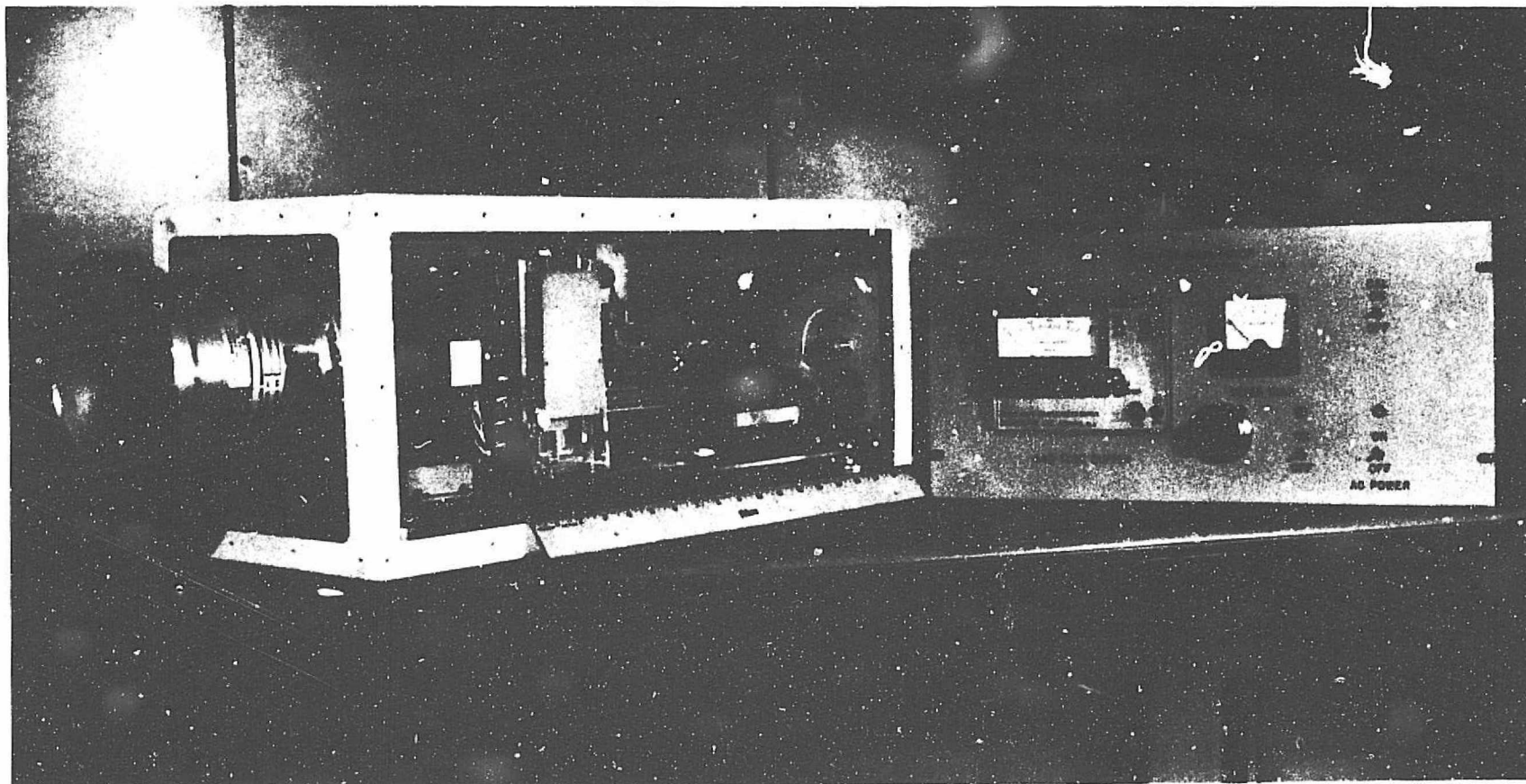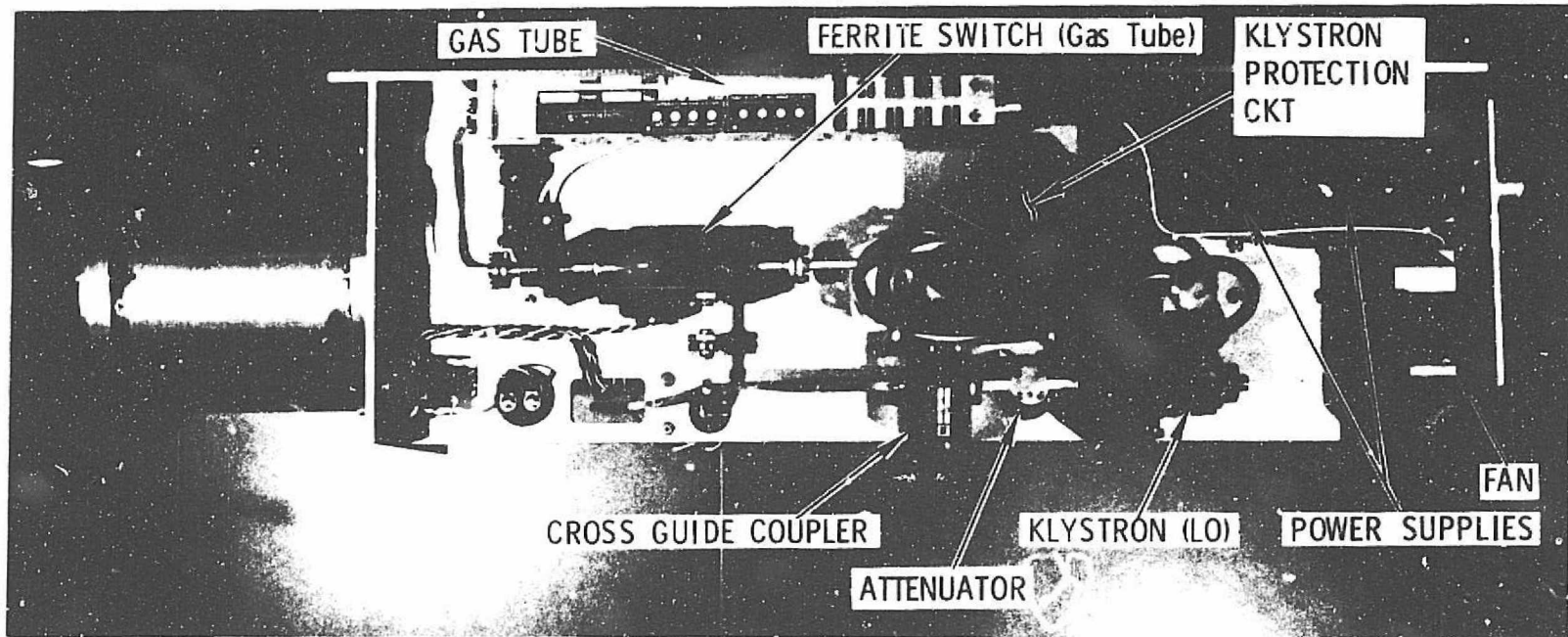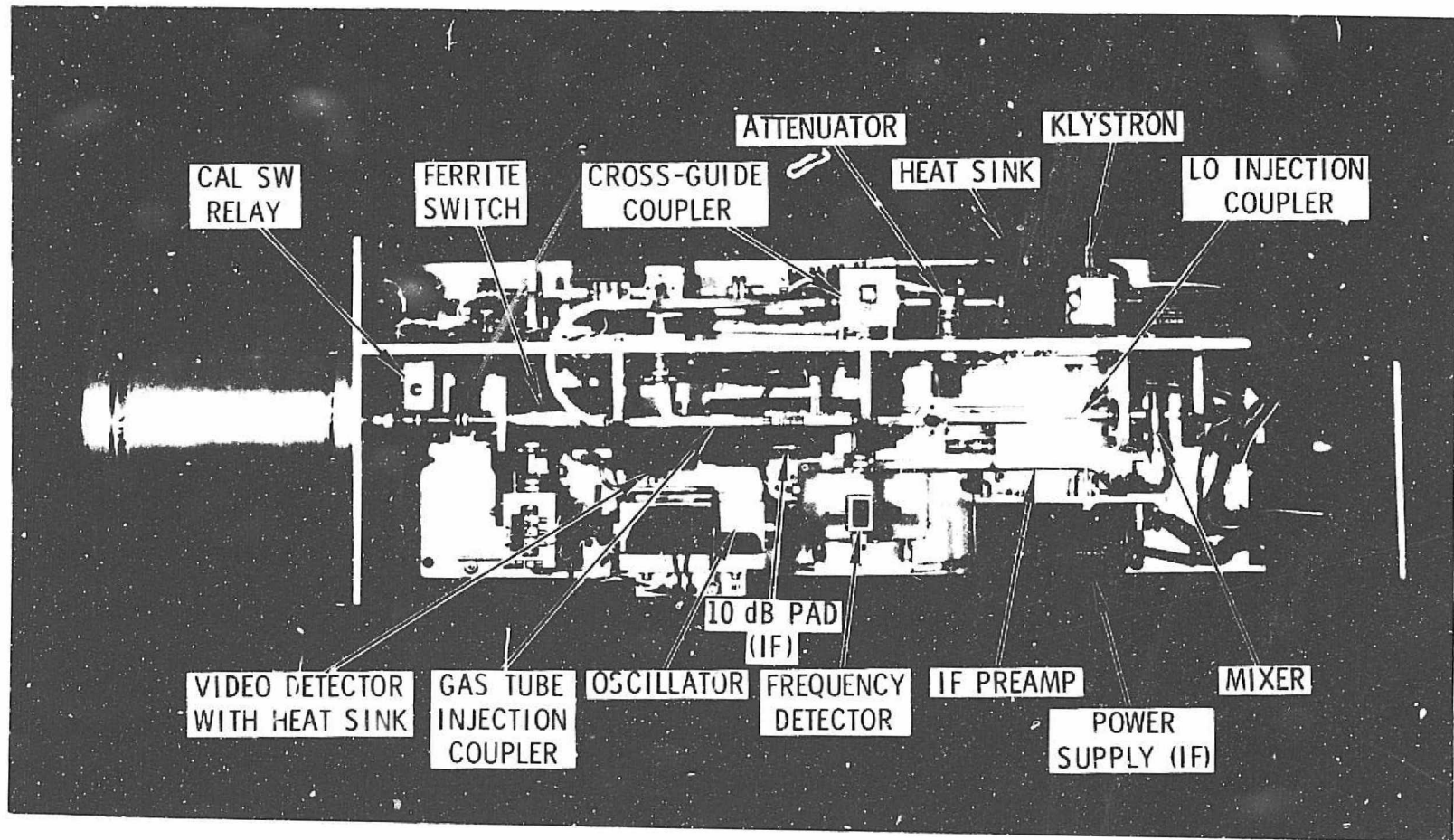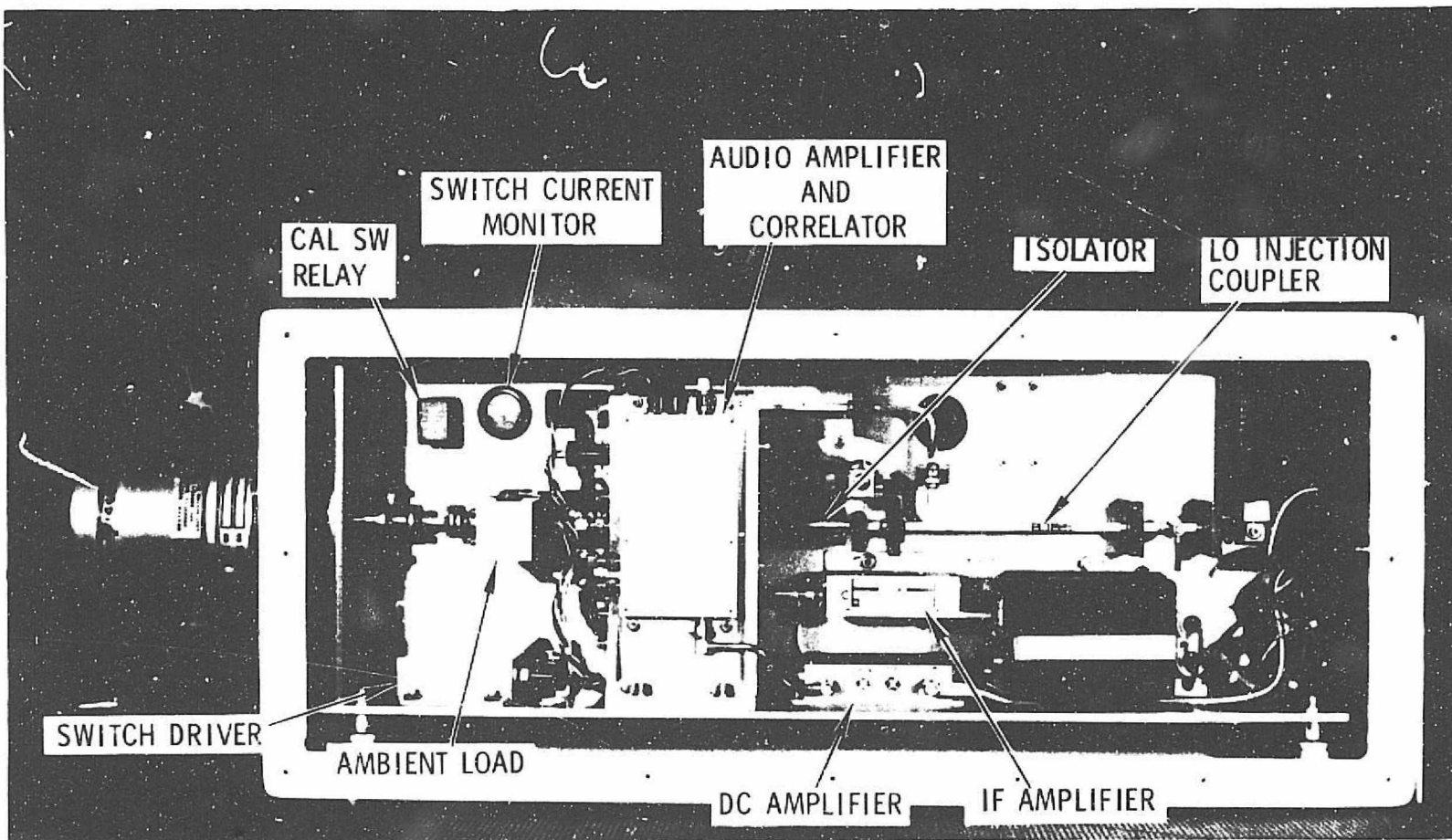Sampling at a rate of 640 samples/second (scans 64° in 0.1 sec) and passing the signals through a 320 cps filter results in a radiometer RMS noise output of 5.57^OK, based on a $\Delta T = 0.22^OK$ (1 sec integration) radiometer. With 4 samples taken for each resolution cell ($2^O \times 2^O$) the net noise is 2.78^OK.

The radiometer output is passed through a low pass filter, sampled at 1^O intervals along the scan, digitized with 12-bit precision and stored in core memory. The shaft angle encoder connected to the mirror axis provides the commands for the sampling. The low pass filter cut-off frequency is 1/2 the sample frequency. The radiometer data, housekeeping, aircraft and calibration data necessary for processing are recorded on a 9-track magnetic tape. A real-time image is available on an airborne oscilloscope monitor and a replay mode is also available.

The on-board monitor gives an immediate image of the data with only 4-bit intensity resolution, in shades of grey. For higher quality images, post-flight processing is done as described by Hollinger, Kenney and Troy (Ref. 13). The software converts the radiometer output to antenna temperature, corrects the aspect ratio of the image for the aircraft speed and altitude, applies the appropriate spatial filtering and smoothing, and presents the image on a TV color monitor. The image consists of 512×512 pixtels with 8-bit intensity resolution and 64 colors available. High resolution color photographs can then be taken of the TV screen and processed as desired. Unfortunately, these beautiful false color images could not be included in this report. In addition, computer printouts of the image data in antenna temperatures are available for extracting the measured target temperatures.

III. OBSERVATIONS

Three flights were made with the 90 GHz radiometer -- December 1974 and two in March 1975. On March 11, the imager was successfully flown on an aircraft at a 3000 ft altitude with over 2000 ft of optically opaque stratus-type clouds beneath the aircraft. The other flights were flown at an altitude of 1500 ft in clear skies. A 35-mm strip-film camera[*] simultaneously photographed the same scene as the radiometer. These strip-film photographs were of poor quality and a photography run, using a high-quality camera, was made on March 18th after an imaging run. Twelve flight lines were chosen to cover a variety of terrain and man-made objects in the vicinity of Wallops Island, Virginia.

A. IMAGES

The raw data from the magnetic tape are displayed on the television monitor of an interactive, computer driven, digital, image display system (Ref. 22). A sample[**] of this display is presented in Fig. 5. It contains the unprocessed image data obtained during a seven minute portion of the December 1974 test flight in the vicinity of Wallops Island. The flight path runs continuously from left to right along each successive row. Increasing brightness temperature corresponds to a grey scale running from white to black. Various terrain features are distinguishable such as cultivated fields and wooded areas in the first row. The bright spot in the left third of the second row is a building with a metal roof which reflects the relatively cold sky and the irregular white region in the center is Little Mosquito Creek. The runway at Wallops Station is next with the white spot on the left end of the runway being a C-54 aircraft. Buildings along the runway appear as lighter regions. Part of the road, causeway, Mosquito Creek, marshland, and Chincoteague Bay follow. Chincoteague Island and the high school and athletic race track appears at the left of the 5th row. The remainder of the flight path passes over farmland, marshland and

---

[*] Flight Research, Model 203-143-4, with 17 mm lens.

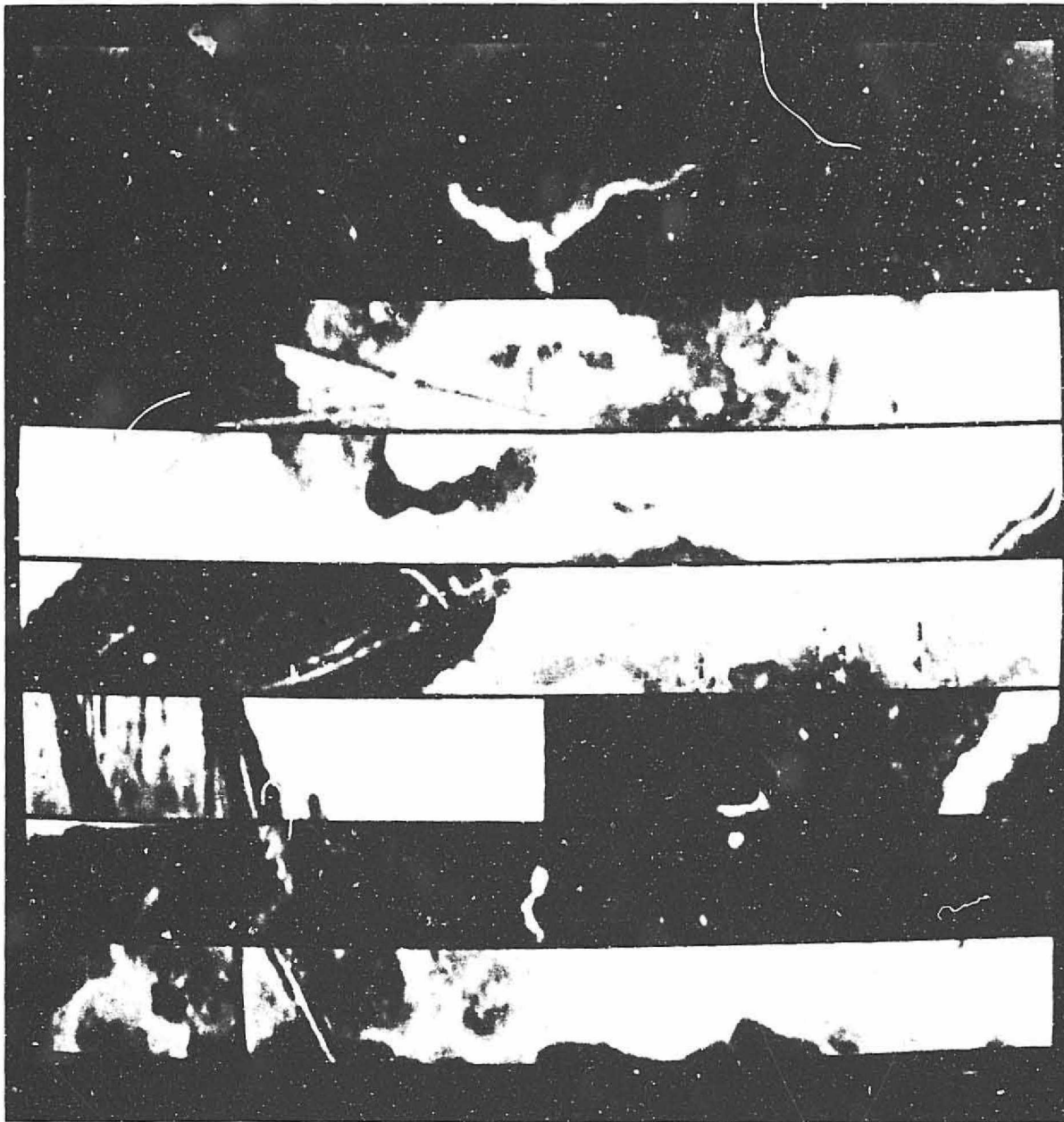[**] Only one was chosen for this report to illustrate a typical display.

Fig. 5.   Unprocessed Imagery Obtained at 90 GHz

-20-

streams of the eastern shore region of Virginia. Any flight can be readily displayed in this manner to provide easy review of all the data obtained. Vertical streaks through some of the frames were caused by RFI from the aircraft communications.

Certain portions of the flight data selected can undergo more detailed analysis as described by Hollinger, Kenney and Troy. Photographic comparisons will be made with a few scenes from these unprocessed radiometric images. Chincoteague Island and the high school are shown in Fig. 6. The corresponding scene taken simultaneously with the 35 mm strip-film camera is also shown. Although the photograph is of poor quality, nevertheless, it points out the significant scenes. Water is shown in the upper left hand corner. The running track which encloses the athletic field is 30 ft wide and is representative of a condition where a good signal-to-noise ratio can resolve a target smaller than the HPBW resolution of 50 ft. Several buildings and various ponds and pools of water may be identified in the 90 GHz image. It is possible that some of the water formations may not be viewed in the photograph or the water may be shadowed by foilage, but the water is enhanced and definitely noticeable in the millimeter wave image.

The Wallops Station runway is shown in Fig. 7. The creek at the left is noticeable in both the image and the photo. The runway features can easily be identified. The aircraft on the left end of the runway is the white spot in the image and is also shown in the photograph. The other bright spot in the image is also an airplane. Both airplanes are C-54s, which have a wing span of 117.5 ft, length 93.83 ft, and body width 10.5 ft.

A water-land scene (Occohannock Creek near Exmore, Va.) is shown in Fig. 8. The bridge or causeway spanning the water is prominent. The water formation shown in the image is more extensive than that indicated in the photograph.

RADIOMETRIC IMAGE

PHOTOGRAPH
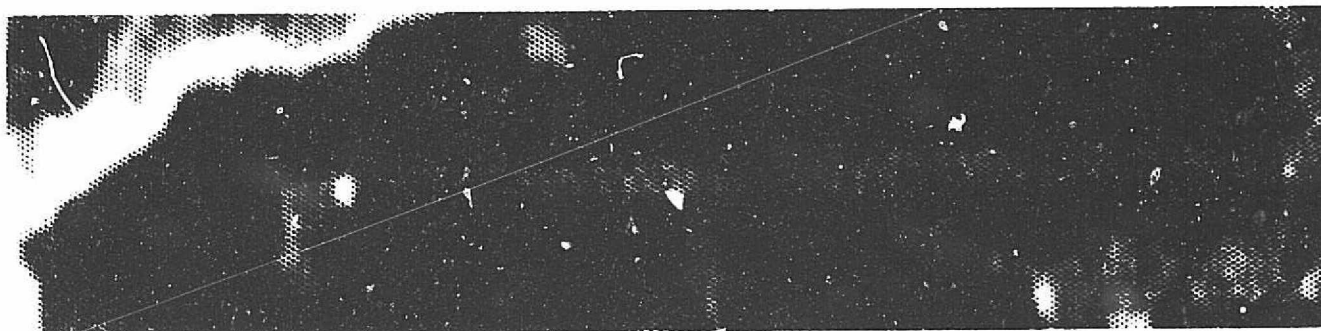

Fig. 6. 90 GHz Radiometric Image of Chincoteague Island and High School

RADIOMETRIC IMAGE
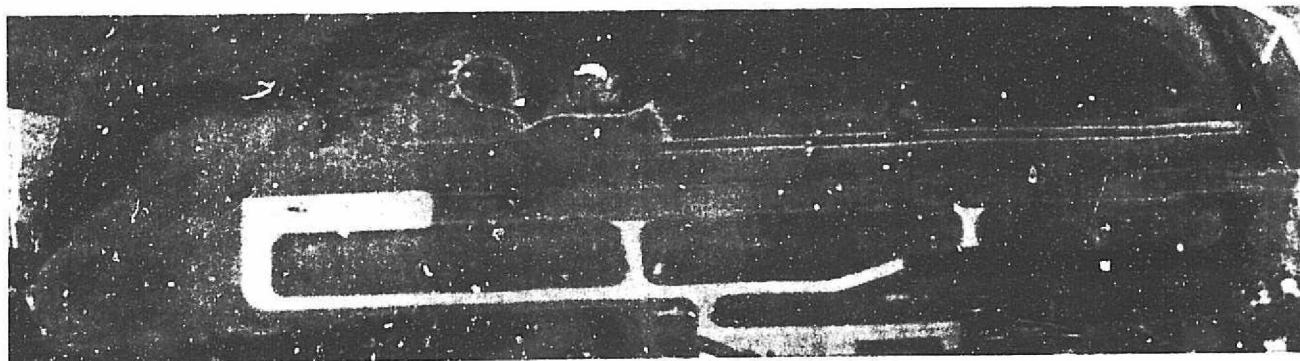
PHOTOGRAPH

Fig. 7.   90 GHz Radiometric Image of NASA Wallops Station

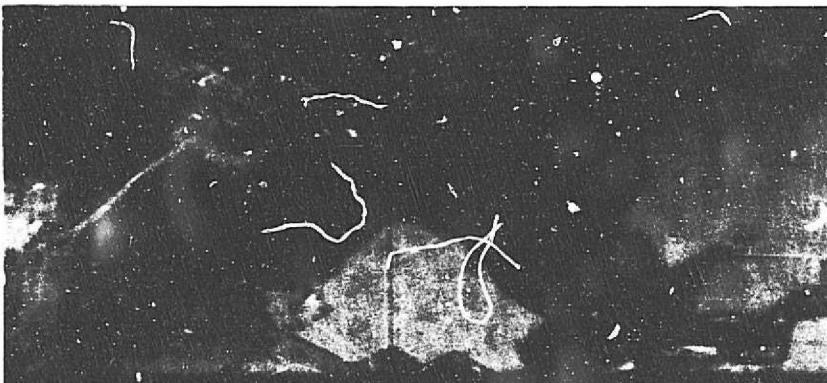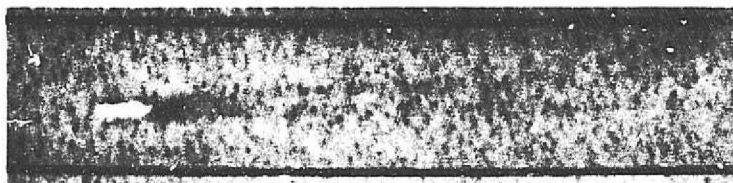**RADIOMETRIC IMAGE**

PHOTOGRAPH

Fig. 8.   90 GHz Radiometric Image of Water-Land Scene

A large ship (~70' ft long, scaled from known land marks from the 35 mm strip-film camera photos) at sea is shown in Fig. 9. The wake is distinguishable in the image. The ship is cold relative to the water (white) and the wake is warmer (darker) than the surrounding water which is expected based on laboratory measurements made by Williams (Ref. 23). The wakes of smaller ships (approximately 425 to 550 ft long) were also noticed in the complete flight image displays, but not presented in this report.

The flight of March 18, 1975 produced an interesting image of the naval shipyards at Newport News, Virginia (Fig. 10). The piers and most of the ships are discernable. A separate photography run was made to take the picture and the resultant slight change in the flight paths during the radiometric scanning caused the different slant angles of the piers.

Many terrain features are identifiable even through 2000 ft of stratus-type clouds. The aircraft was flown at an altitude of 3000 ft, with broken clouds from 800 to 1100 ft, solid clouds from 1100 to 2800 ft. The outside ambient temperature = $0^{\circ}C$, 800 to 1800 ft, $0^{\circ}C$ to $1.5^{\circ}C$, 1800 to 2800 ft. Figure 11(a) shows the radiometric image, as seen through clouds, of the Assateague and Chincoteague Islands. The causeway and bridge connecting the two islands are clearly visible in the image. Other land formations, marshland, and waterways are resolved. Photography was not possible during this run because of the opaque clouds. However, a portion of the U.S. Coast and Geodetic Survey map (Chincoteague East Quadrangle, Virginia, Accomak Co., Topographic, 1965) is shown for comparison with the image. The harbor at Chincoteague and the island within Sheepshead Creek can be seen in the image of Fig. 11(b). The radiometric images of Fig. 11 are unprocessed and uncorrected for aspect ratio; i.e., the image should have been expanded in width by a factor of 2.

RADIOMETRIC IMAGE
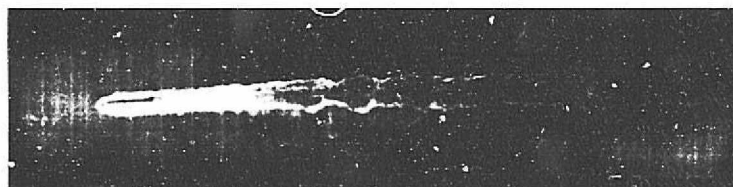
PHOTOGRAPH

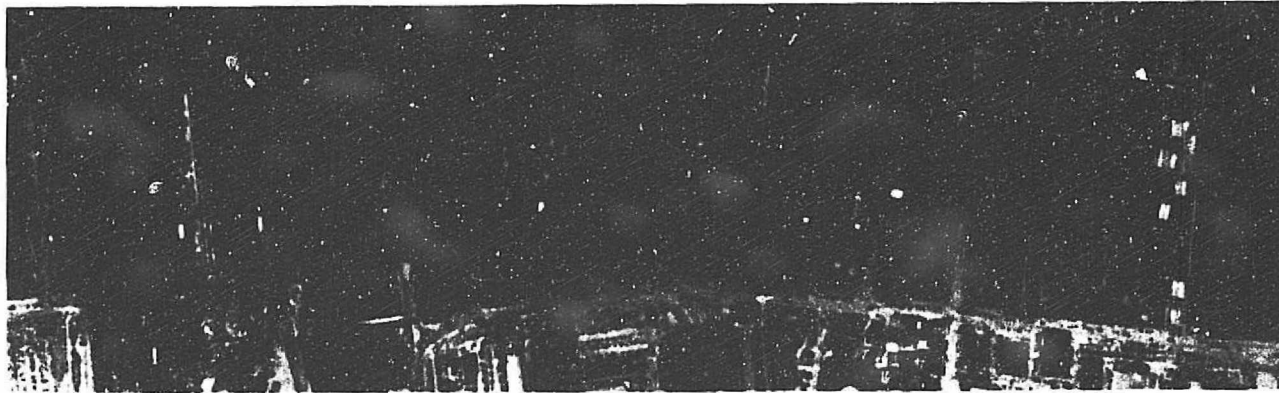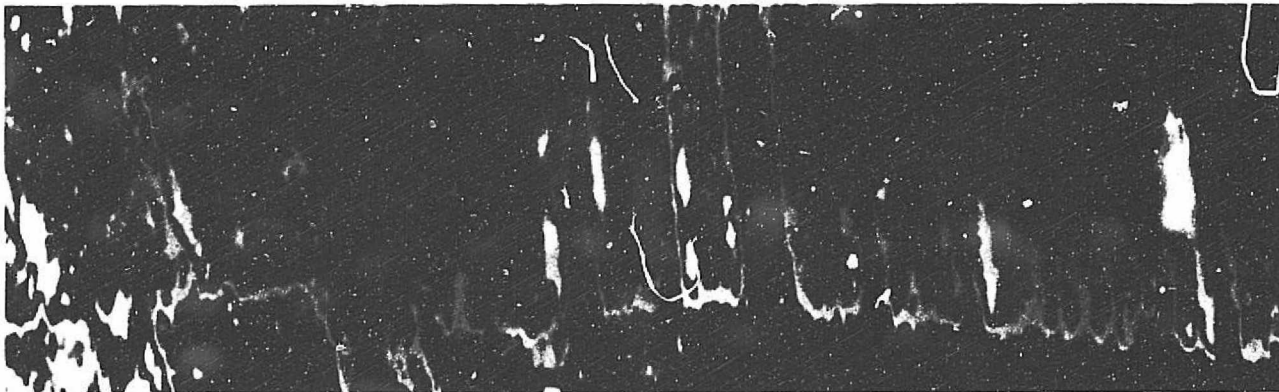Fig. 9.   90 GHz Radiometric Image of Ship and Wake

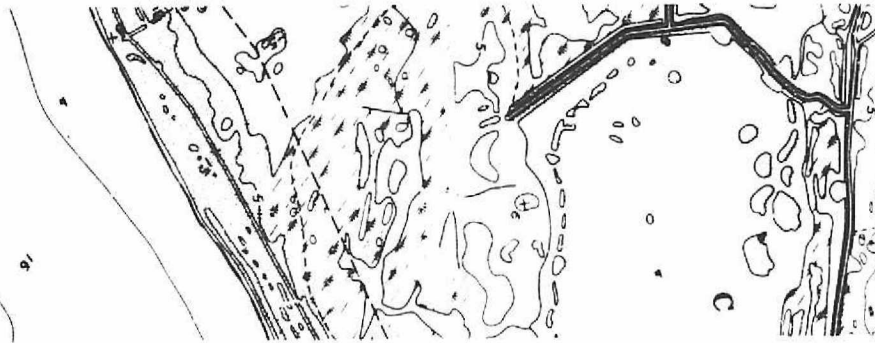**PHOTOGRAPH**

RADIOMETRIC IMAGE

Fig. 10.   90 GHz Radiometric Image of Naval Shipyard at Newport News, Va.

RADIOMETRIC IMAGE

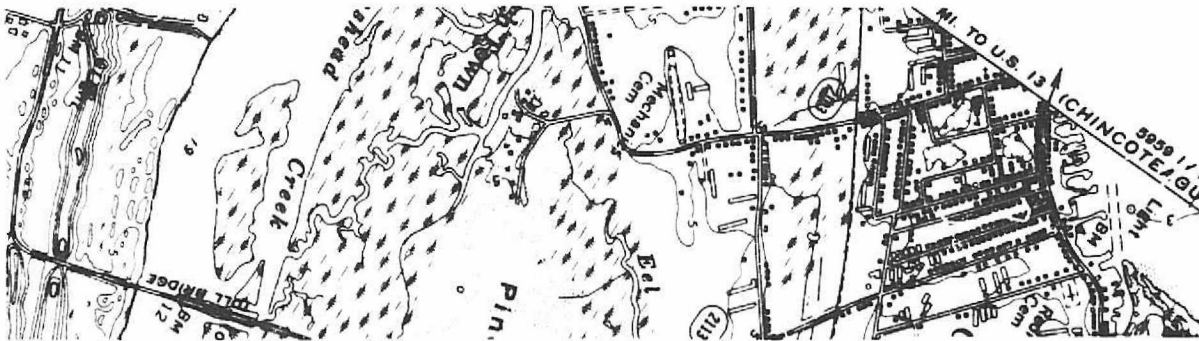Image width compressed by a
factor of 2:1

GEOLOGICAL SURVEY MAP

(a) Assateague Island

RADIOMETRIC IMAGE

GEOLOGICAL SURVEY MAP

(b) Chincoteague Island

Fig. 11. 90 GHz Radiometric Images Through Cloud Cover

-28-

B. TARGET ANTENNA AND BRIGHTNESS TEMPERATURES

1. Measured Antenna Temperatures

Using the printout listings of the unprocessed antenna temperatures, the distribution of antenna temperatures over a relatively uniform terrain sample are plotted in Fig. 12. The temperature distribution of vegetation includes samples from the grassland between the runway and the river at Wallops and from an area in the vicinity of the Chincoteague High School. They were combined since there are no systematic differences between the two samples. The distribution of the temperatures for concrete are taken from the creek end (left) of the runway at Wallops. Both the vegatation and concrete distributions have a standard deviation (1σ) of $< \pm 4^\circ K$. The radiometer output noise fluctuations of $2.78^\circ K$ accounts for part of this variation. Atmospheric variations could also account for some of the spread. Sea water has more scatter in its distributions due to its variable emissivity, sea state, and surface turbulence. The true sea state and other parameters such as surface winds, foam cover, and wave height were not established during these measurements. Composite sites, like docks and towns show larger spreads in the observed temperatures. Ships show wide, non-Gaussian scatter. It was noted that ships at sea were colder than those at the docks.

Antenna temperature profiles of a ship and its wake (the one of Fig. 9) are shown in Fig. 13. The midregion of the ship shows the cooler ship with respect to the water. The wake immediately aft of the ship is shown warmer and as the wake trails off the spread of the wake can be seen.

Table 1 shows the tabulated temperatures of targets of interest. The 14 and 19 GHz temperatures were recorded simultaneously with the March 18, 1975 90 GHz clear-day imaging flight. These values assumed that the ambient temperature = $290^\circ K$.
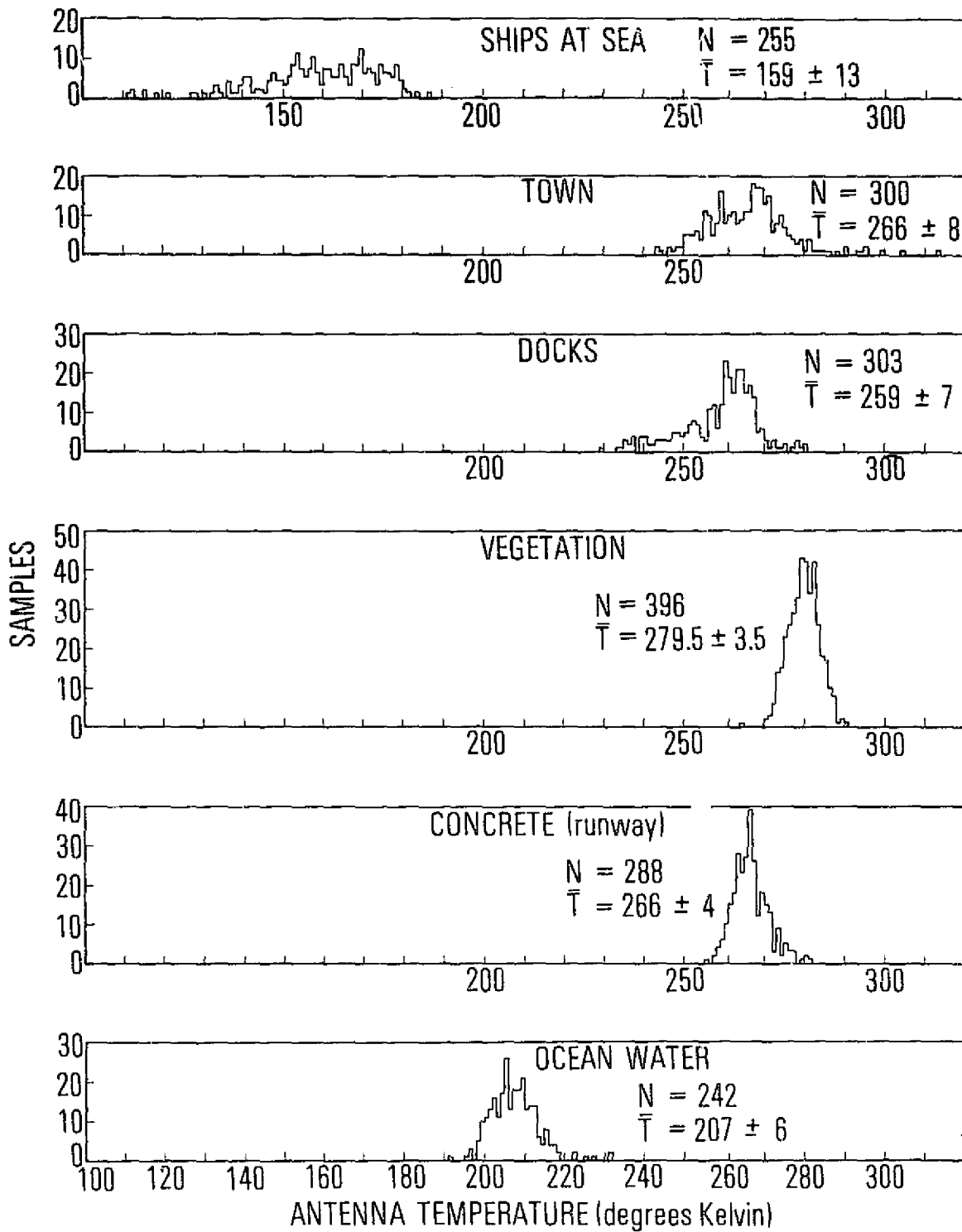
Fig. 12.   Temperature Distribution of Various Targets
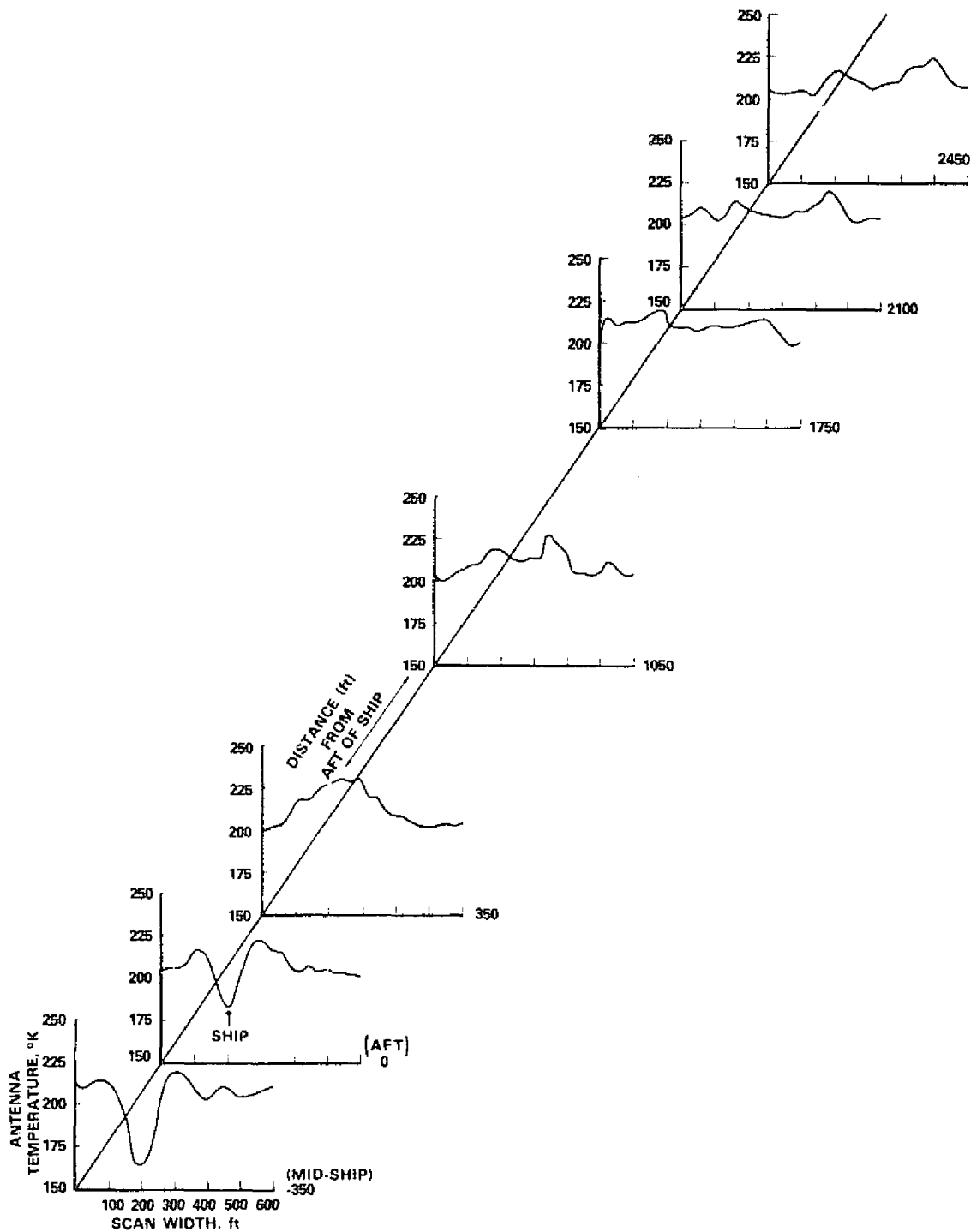
Fig. 13. Temperature Profiles of Ship and Wake

TABLE 1

ANTENNA TEMPERATURES OF SELECTED TARGETS

Targets	Temperature, °K		
	Frequency		
	14 GHz	19 GHz	90 GHz
Vegetation	237 ± 16 N = 12	239 ± 11 N = 12	279.5 ± 3.5 N = 396
Concrete (Runway)	———	———	266 ± 4 N = 288
Docks	190 ± 11 N = 4	189 ± 5 N = 4	259 ± 7 N = 303
Ocean Water	105 ± 6 N = 14	114 ± 3 N = 16	207 ± 6 N = 242
Ships at Sea	———	———	159 ± 13 [*] N = 255
Ships at Dock	80 N = 1	< 100 N = 1	168 ± 12 [**] N = 168
C-54 Aircraft (on Runway)	———	———	225 ± 9 N = 18

N = number of samples

1 σ = ± values

[*]   4 ships, 425 ft to 708 ft lengths

[**]   5 ships, 250 ft to 750 ft lengths

2.   Brightness Temperature

The determination of the brightness temperature of a ground target from airborne-sensor antenna temperature measurements is difficult because of the influence of atmospheric emission, atmospheric attenuation, target thermometric temperature, antenna pattern and losses, and the target non-specular reflection characteristics. If the atmosphere were transparent and with an ideal antenna pattern for target sensing, the brightness temperature is equivalent to the measured antenna temperature. To extract the brightness temperature of the surface from the antenna temperature, one can apply Fourier transform techniques as described by Homes, Balanis and Truman (Ref. 24). For a preliminary analysis, Appendix A provides a simplified model to acquire an approximation of the brightness temperature from the measured antenna temperature. It also illustrates the contributing temperatures that are combined to obtain the antenna temperature.

A radiometric system designer is usually interested in the brightness temperature = ϵT, where ϵ = emissivity of the material and T = physical temperature of the material. If the emissivity of materials were known, then brightness temperatures can be predicted reasonably well from the physical temperature. However, the emissivity is difficult to predict for different types of terrain because it is a complex function of numerous material properties (dielectric constant, conductivity, surface roughness, sub-surface composition, surface orientation) and also the observation frequency, polarization and incidence angle affects the emissivity characteristics. At the millimeter wave frequencies, targets are typically random (rough-surface or diffuse) reflectors rather than specular reflectors. Because of the complexity of specifying emissivity, this initial report presents the measured antenna temperatures. From these measurements, the apparent brightness temperature or apparent emissivity can be inferred from Eq. A-11 (Appendix A).

Figure 14 shows the antenna temperature as a function of the emissivity ϵ using Eq. A-11 and Eq. A-13, which accounts for the antenna losses. The sensor is specified at 1500 ft altitude (target at ground or sea level), zero zenith angle, and for a dry, average and humid clear day. The antenna characteristics are for the horn-lens antenna used in the flight radiometer which has a beam efficiency = 97% and an insertion loss = 0.35 dB, based on data supplied by TRG[*]. Note that on an average clear day, where the zenith atmospheric attenuation is 0.84 dB, that the minimum antenna temperature (for ϵ = 0) is 79°K, with the reflecting sky temperature ($\sim$48°K) contributing a major portion of the signal. Under ideal radiometric measuring conditions, the brightness temperature = 0°K for ϵ = 0. In contrast, when ϵ = 1, the sensor essentially sees the actual target temperature attenuated by the loss in the medium between the ground and the airborne sensor, assuming no contribution from the reflecting sky temperature.

The antenna temperature, as a function of the emissivity, ϵ, for a cloudy day is also shown in Fig. 14. The condition was similar to the cloudy-day flight of March 11, 1975, with the aircraft at 3000 ft, assuming 3 dB attenuation in the clouds, cloud temperature[**] = 280°K, and average water vapor content above the aircraft. It confirms that there is sufficient contrasting antenna temperatures to measure different types of targets, as experienced on the cloudy-day flight. However, as the cloud attenuation increases, the antenna temperature will approach ambient temperature, resulting in the inability to discern contrasting target temperatures.

---

[*] G. J. Gill, Computer Data Corporation, Microwave Products Division, Formerly TRG, Inc., Antenna Model W-858-6.

[**] Temperature at cloud altitudes was recorded as $\sim$273°K, but 280°K was chosen as an average from ground level to 3000 ft.
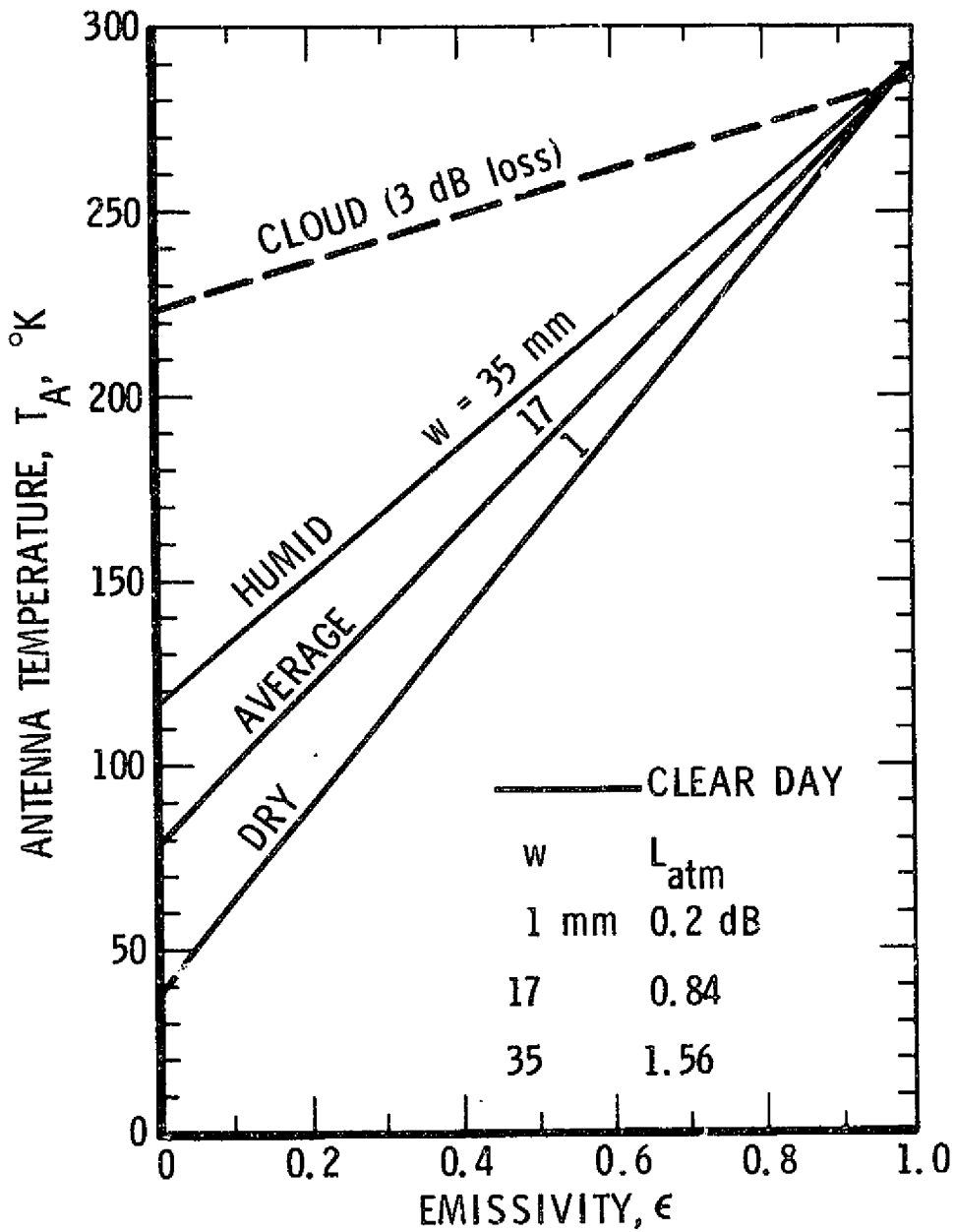
Fig. 14.   Antenna Temperature of Sensor at 1500 ft Altitude on a Clear Day and at 3000 ft for a Cloudy Day as a Function of Ground Emissivity.

IV. APPLICATIONS

The 90 GHz radiometric images presented herein represent the first known measurements performed for the purpose of detecting relatively small targets. The images made through optically opaque clouds (2000 ft thick) illustrate some interesting potential uses of 90 GHz passive imagery for both civil and military applications.

A. CIVIL

1. Forest Service

The strategy in fighting forest fires requires knowledge of the status of the fire over a large area; i.e., whether it's an open fire, a smoldering fire, ember fire or burnt-cut fire. Survey of the fire situation is often hampered by clouds and smoke. The characteristics that make 3 mm radiometric imaging attractive for the forest service are as follows:

- Ability to see through clouds

- Potential capability to see through smoke

- Roads, fire-breaks, lakes, streams are distinguishable

- Status of fires can be detected, because of the varying thermometric temperatures of an open fire, smoldering fire, ember fire, and burnt-out fire

- Terrain with wet or dry soil or foliage can be resolved which aids fire fighters to recognize potentially dangerous dry areas.

2. Aeronautical Navigation

The ability of the 90 GHz imager to see through clouds makes millimeter wave radiometry technically feasible for airborne navigation. Its use as a navigational aid was proposed by Mayer (Ref. 25). Successful enroute navigation requires well-known reference maps, which must account for fluctuations from seasonal and diurnal weather and other factors. Such fluctuations may limit the utility of map-matching techniques which must compete

Preceding page blank

with present navigational systems. What constitutes a "well-known" map
has to be determined with additional flights and research. For the observers
on the March 11, 1975 cloudy-day flight, it was an impressive sight to fly
over optically opaque clouds and see the roads, rivers, lakes and other land
formation on the real-time image TV monitor. It is technically feasible for
radiometric maps to supplement instrument landing systems or ground traf-
fic control systems, particularly during foggy or cloudy days.

3.   Law Enforcement Aid

Law enforcement groups often have the need to search and track ground
targets from the air under foggy, cloudy and night conditions. Millimeter wave
radiometers offer this potential. A very likely application is to use airborne
imaging systems to follow automobiles, to search out marshlands for hidden
boats, and to locate automobiles hidden underneath foliage.

4.   Ice Formation

New ice and old ice have different emissivities and therefore, different
brightness temperatures. With a high resolution millimeter wave imaging
system, the formation of ice and the ice boundaries can be detected. Such
information is useful to determine the potential opening and closing of ship-
ping lanes.

5.   Meteorological Sensing

An airborne or satellite-borne imaging system can be utilized to map
out the earth's weather fronts and detect clouds, fog, rain, snow, sleet, and
ice formation. Application to meteorological systems have been discussed in
the Introduction; however, there are no active plans utilizing 90 GHz or 140 GHz
radiometers.

B.   DEFENSE

1.   Terminal Guidance

Millimeter wave passive imaging systems are able to distinguish
bridges, roads, streams, lakes, shorelines, cultivated lands, wooded areas,
runways, piers, ships in dock and other prominent land marks even through
cloud cover. Terminal guidance systems using map-matching techniques

with passive sensors appear to be technically feasible. Maps can be synthe-
sized from reconnaissance photographs or millimeter-wave images. By cor-
relating an entire frame or field-of-view with a reference map reliable error
signals may be obtainable for terminal guidance.

2.   Tactical Warfare

With the ability of 90 GHz radiometers to detect aircraft, ships, build-
ings, and other land formations, imaging systems can be used for a number of
situations:

- Surveillance of air bases to make an aircraft count

- Search of land areas for convoys of tanks, trucks and other
  military vehicles. The build-up and movement can be de-
  tected.

- Search of sea for ships

- Potential location of submarines, although the detection of
  submarines and their wake has not been demonstrated

- Search of swamp land hidden optically by foliage and to seek
  out concealed boats in these waters

- Search for other tactical targets such as missile silos, rail-
  road centers/depots, ammunition dumps, petroleum and oil
  storage areas, factories, harbors and cities.

It should be emphasized that the reconnaissance can be done under cloudy or
night conditions.

3.   Post-Attack Assessment

A baseline of millimeter wave imaging data for various geographical
locations and targets could provide a passive method for assessing an attack.
The assessment can be done at night or under cloudy conditions. Flights
would be made to a location after an attack to determine the extent of the
damage, or after a ship has been destroyed at sea.

V. CONCLUSIONS

An airborne versatile millimeter wave imaging system with a ground resolution of 50 ft was found to be practical. The 90 GHz radiometer has a $\Delta T = 0.22^{\circ}K$ for a 1 sec integration time. The radiometer system was flown in a NASA airplane. The antenna-beam mechanical scanning mirror was scanned at a rate of $640^{\circ}/sec$ over an angle of $\pm 32^{\circ}$ from nadir forming a zigzag track across the ground with aircraft motion. The resultant radiometer noise fluctuation is $2.78^{\circ}K$ per resolution cell. Aircraft flights with the imaging system produced real-time images under clear and cloudy weather. Post-flight data processing provides higher quality images. Looking through 2000 ft of clouds, the imaging system clearly distinguished waterways, roads, bridges and other land forms. On a clear day, it was possible to resolve ships and their wakes, aircrafts on the ground, athletic fields, cultivated land and wooded areas. Targets smaller than the antenna halfpower beamwidth resolution cell were discernable. Water formations found in radiometric images were not always obvious from the photographs; i.e., foliage may have restricted the viewing of the water optically. Many factors such as atmospheric emission, ground temperatures, antenna performance, target reflection characteristics, and intervening medium between target and sensor, must be accounted for to determine brightness temperatures from the measured antenna temperatures.

Preceding page blank

VI.   REFERENCES

1.   K. Tomiyasu, "Remote Sensing of the Earth by Microwaves", Proc. IEEE, 62, 86-92, January 1974.

2.   J. W. Waters, F. T. Barath, E. Y. Chow, A. F. H. Goetz, E. J. Johnston, J. M. Stacey, J. J. Gustincic, D. H. Staelin, J. A. Kong, E. G. Njoku, K. F. Kunzi, D. O. Muhleman, and T. T. Wilheit, "The Shuttle Imaging Microwave System Experiment", IEEE National Telecommunications Conference, New Orleans, December 1-3, 1975. (Proceedings)

3.   G. T. Wrixon, "Measurements of Atmospheric Attenuation on an Earth-Space Path at 90 GHz using a Sun Tracker", Bell System Technical Jl, 50, 103-114, January 1971.

4.   L. I. Lo, B. M. Fannin, A. W. Straiton, "Attenuation of 8.6 and 3.2 mm Radio Waves by Clouds", IEEE Trans. on Antennas and Propagation, AP-23, 782-786, November 1975.

5.   T. T. Wilheit, "The Electrically Scanning Microwave Radiometer (ESMR) Experiment", The NIMBUS-5 User's Guide, NASA Goddard Space Flight Center, Greenbelt, Maryland, pp. 59-105, 1972.

6.   T. T. Wilheit, "The Electrically Scanning Microwave Radiometer (ESMR) Experiment", NIMBUS-6 User's Guide, NASA Goddard Space Flight Center, Greenbelt, Maryland, pp. 87-108, 1975.

7.   D. H. Staelin, A. H. Barrett, P. W. Rosenkranz, F. T. Barath, E. J. Johnston, J. W. Waters, A. Wouters, "The Scanning Microwave Spectrometer (SCAMS) Experiment", The NIMBUS-6 User's Guide, NASA Goddard Space Flight Center, Greenbelt, Maryland, pp. 59-86, 1975.

8.   P. Gloersen, "Description of a Mechanically Scanned Microwave Radiometer for Use on NIMBUS-G", NASA Goddard Space Flight Center, Greenbelt, Maryland, 1973.

9.   "Microwave Imager Sensor Study (MISS)", SAMSO TR in publication.

References (continued)

10. M. F. Schneider, C. J. Vesely, "A Description of the DMSP Passive Microwave Temperature Sounder", Opt. Soc. Amer. Technical Digest on Remote Sensing of the Atmosphere, 1975.

11. J. P. Hollinger, "Passive Microwave Measurements of Sea Surface Roughness", IEEE Trans. on Geoscience Electronics, GE-9, 165-169, July 1971.

12. J. P. Hollinger, "The Determination of Oil Slick Thickness by Means of Multifrequency Passive Microwave Techniques", Final Report, Naval Research Laboratory, Report No. NRL-MR-2953, AD A001302, 30 June 1974.

13. J. P. Hollinger, J. E. Kenney, and B. E. Troy, "A Versatile Passive Microwave Imaging System", IEEE Trans. on Antennas and Propagation, submitted for publication.

14. W. A. Johnson, "Performance of a 3.3 mm Radiometer", Electronics Research Laboratory, The Aerospace Corporation, Report No. TR-0158(3230-46)-13, February 1968. Also, IEEE Trans. on Microwave Theory and Techniques, MTT-16, 621-625, September 1968.

15. C. J. Carter, R. L. Mitchell, and E. E. Reber, "Oxygen Absorption Measurements in the Lower Atmosphere", J. Geophys. Res. 73, 3113-3120, May 1968.

16. W. A. Johnson, T. T. Mori, and F. I. Shimabukuro, "Design, Development, and Initial Measurements of a 1.4-mm Radiometric System", IEEE Trans. on Antennas and Propagation, AP-18, 512-514, July 1970. Also, The Aerospace Corporation, Electronics Research Laboratory Technical Report No. TR-0066(5230-48)-1, February 1970.

17. W. J. Wilson, P. R. Schwartz, E. E. Epstein, W. A. Johnson, R. D. Etcheverry, T. T. Mori, G. G. Berry, and H. B. Dyson, "Observations of Galactic Carbon Monoxide Emission at 2.6 Millimeters", Astrophy. J. 191, 357, 15 July 1974.

18. F. I. Shimabukuro, W. J. Wilson, P. L. Smith, "Estimation of the Ozone Distribution from Millimeter Wavelength Absorption Measurements", J. Geophys. Res. 80, 2957, 1975.

References (continued)

19.   W. J. Wilson, T. T. Mori, J. W. Montgomery, H. E. King, "The Aerospace Corporation's Millimeter Wave Spectral Line Receiver", (Abstract) URSI, Comm. V Meeting Proceedings, October 1974.

20.   G. T. Chalfin and W. B. Ricketts, "3.2-mm Thermal Imaging Experiments", in Proc. 4th Symp. Remote Sensing of Environment, pp. 859-871, Ann. Arbor, Michigan, April 1966.

21.   R. D. Etcheverry, W. A. Johnson, and T. T. Mori, "Properties of GaAs Schottky Mixers at 3.2-mm", The Aerospace Corporation, Electronics Research Laboratory Technical Report No. TR-0172 (2230-20)-12, 30 March 1972.

22.   I. Jurkevich, J. Lee, and A. F. Petty, Naval Research Laboratory. Display System Report in preparation, 1975.

23.   G. F. Williams, "Microwave Emissivity Measurements of Bubbles and Foam", IEEE Trans. on Geoscience Electronics, GE-9, 221-224, October 1971.

24.   J. J. Homes, C. A. Balanis, W. M. Truman, "Application of Fourier Transforms for Microwave Radiometric Inversions", IEEE Trans. Antennas and Propagation, AP-23, 797-806, November 1975.

25.   A. Mayer, "Target Contrast Considerations in Millimeter Wave Radiometry for Airborne Navigation", Ames Research Center, Moffett Field, California, NASA TM-X-62, 082, August 1971.

APPENDIX A

ANTENNA AND BRIGHTNESS TEMPERATURE RELATIONS

The target brightness temperature (ϵT) cannot be precisely derived from the measured antenna temperatures because of the effects of atmospheric emission and attenuation, target temperature, antenna pattern and the target non-specular reflection characteristics. In the absence of any atmospheric absorption and no extraterrestrial signal reflected by the target into the sensor, the antenna temperature with an ideal antenna pattern is equivalent to the target brightness temperature. This Appendix will show the typical contribution from the various factors illustrated in the ideal model of Fig. A-1. Radiation from all parts of sky is actually reflected toward the sensor, but the simlified model will provide a first-order estimate of the antenna temperatures. The atmospheric model has been simplified by assuming a constant temperature-height profile and the precipitable water vapor and oxygen profile varies expontially with height (Refs. A-1 and A-2). Antenna temperature equations will be presented followed by a sample calculation using the sensor antenna described in this report.

The antenna temperature is composed of 4 basic terms:

1. Brightness temperature ϵT of target attenuated by the atmosphere between target and sensor

$$= \epsilon T \, e^{-\tau_{GA} \sec z} \tag{A-1}$$

2. Emission from the atmospheric medium between target and airborne sensor

$$= T_{GA} \, (1 - e^{-\tau_{GA} \sec z}) \tag{A-2}$$
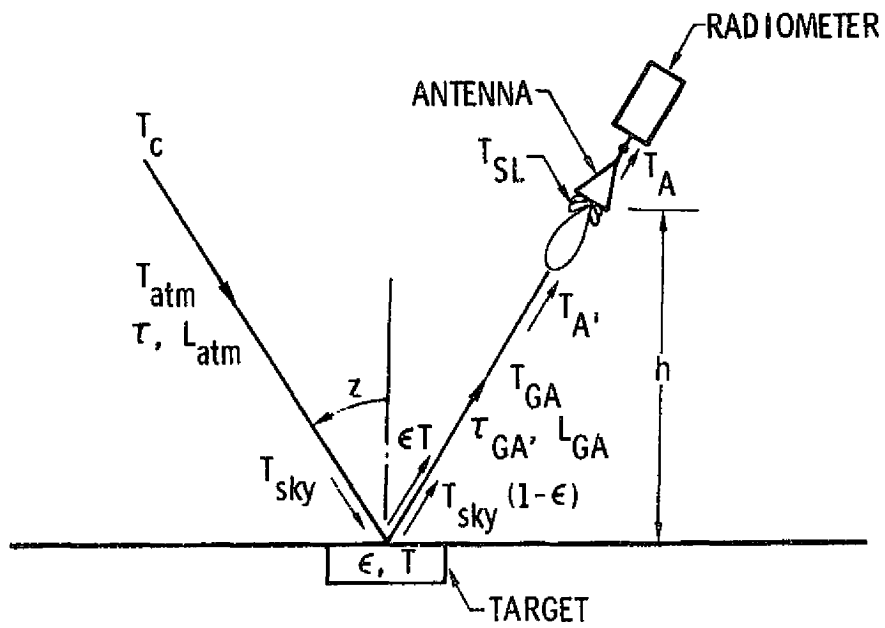
Preceding page blank

Fig. A-1.   Antenna Temperature Model

3. Incident sky temperature, T_{sky}, reflected by target and attenuated from the ground level to the aircraft

$$= T_{sky}(1 - \epsilon) \, e^{-\tau_{GA}\sec z} \qquad (A-3)$$

$$= \left[T_c \, e^{-\tau \sec z} + T_{atm}(1 - e^{-\tau \sec z}) \right] (1-\epsilon)e^{-\tau_{GA}\sec z} \qquad (A-3a)$$

4. Atmospheric emission and background entering the sidelobes and backlobes of antenna, is

$$= (1 - \eta_B) \, T_{SL} \qquad (A-4)$$

The signals received from the first 3 terms are assumed to be received by the antenna's main beam; therefore, the 3 terms are multiplied by the solid-angle main beam efficiency, η_B (Ref. A-3). Therefore, the sensor antenna temperature at the antenna aperture, is

$$
T_A' = \left\{ \epsilon T \, e^{-\tau_{GA}\sec z} + T_{GA} (1 - e^{-\tau_{GA}\sec z}) \right.
$$
$$
\left. + \left[T_c \, e^{-\tau \sec z} + T_{atm} (1 - e^{-\tau \sec z}) \right](1-\epsilon) e^{-\tau_{GA}\sec z} \right\} \eta_B
$$
$$
+ (1 - \eta_B) \, T_{SL} \qquad (A-5)
$$

where ϵ = emissivity of target

T = physical temperature of target

T_{atm} = average temperature of atmosphere from sea level to the exosphere = 280°K

T_{GA} = temperature of atmosphere from ground level to aircraft

T_c = cosmic blackbody background temperature = 2.7°K

T_{SL} = temperature entering sidelobes and backlobes of antenna

τ = opacity of entire atmosphere

τ_{GA} = opacity of medium intervening between target and aircraft

η_B = solid angle main beam efficiency (between first pattern nulls)

z = zenith angle

The terms $e^{-\tau \sec z}$ and $e^{-\tau_{GA} \sec z}$ are transmissivities of the atmosphere for different path lengths which are related to loss terms as

$$L_{atm} = e^{\tau \sec z} \qquad (A-6)$$

$$L_{GA} = e^{\tau_{GA} \sec z} \qquad (A-7)$$

A transmission loss factor L is generally used in expressing transmission loss through lossy microwave circuits and can be applied to a terrestrial media (Ref. A-4).

At 90 GHz, the total atmospheric loss (Refs. A-5 and A-6) in the zenith direction is

$$L_{atm} = 0.16 + 0.04w \quad dB \qquad (A-8)$$

where w = precipitable water vapor in mm. The 0.16 factor is due to oxygen absorption. E.g., the atmospheric loss for various values of w, are as follows:

w mm	Condition	L, dB water	L, dB oxygen	L_{atm}, dB Total
1	Dry	0.04	0.16	0.20
17	Average	0.68	0.16	0.84
35	Humid	1.40	0.16	1.56

The attenuation from a height (h) to outer space, assuming that the attenuation varies exponentially with altitude above sea level can be approximated by

$$L(h) = L(h=0)_{dB} \; e^{-h/h_s} \quad\quad dB \quad\quad\quad (A-9)$$

and

$$L(h) = L(h)_{oxy} + L(h)_{water}$$

where h = altitude of interest

h_s = scale height.

= 1.5 to 2 km for water vapor depending upon the value of w (Ref. A-1)

= 5.4 km for oxygen (Ref. A-2)

The loss from the ground level to the aircraft is

$$L_{GA} = L_{atm}(1 - e^{-h/h_s}) \quad\quad dB \quad\quad\quad (A-10)$$

The loss factors for L_{GA} are:

w mm	Scale Height h_s, km water	L_{GA} water dB	L_{GA} total dB
1	1.5	0.011	0.024
17	1.5	0.179	0.192
25	1.7	0.330	0.343

$$L_{GA} \; (oxygen) = 0.013 \; dB$$

Rewriting Eq. A-5, assuming z = 0, and using the transmission loss factors (Eqs. A-6 and A-7), the sensor antenna temperature at the antenna aperture is

$$T_A' = \left\{ \frac{\epsilon T}{L_{GA}} + T_{GA}\left(1 - \frac{1}{L_{GA}}\right) + \left[\frac{T_c}{L_{atm}} + T_{atm}\left(1 - \frac{1}{L_{atm}}\right) \right] \frac{1 - \epsilon}{L_{GA}} \right\} \eta_B$$

$$+ (1 - \eta_B) T_{SL} \quad\quad\quad (A-11)$$

$T_{atm} = 280^{\circ}K$, an average chosen for the temperature where most of the attenuation takes place.

The beam efficiency, $\eta_B = 97\%$, is the value for the flight radiometer horn-lens 6-in. aperture antenna[*]. It is assumed that the antenna radiation patterns are the same with and without the scanning mirror (Ref. 13). The angle to the first null was selected as 3°. Thus, beam efficiency means that 97% of the power is contained within $\pm 3^{\circ}$ of the antenna beam boresight axis; or, 3% of the power is radiated outside the main lobe into the sidelobes and backlobes. The TRG data also show that 99.9% of the power is radiated within $\pm 10^{\circ}$ of the beam maximum. The major sidelobes (2.9% of power) look at the surroundings of the target. If the remaining sidelobes and backlobes (0.1% power) look at the surrounding ambient temperature of 290°, their contribution is $< 0.3^{\circ}K$.

For broad targets the close-in sidelobes essentially see the same scene as the main beam. For targets with a temperature gradient, the sidelobes will be looking at varying temperatures -- possible hotter on one side of the beam and cooler on the opposite side. Whatever the case may be, the maximum contribution is 2.9% of the surrounding ambient temperature or $0.029 (290) = 8.7^{\circ}K$. For the example, T_{SL} will be assumed to be identical to the temperature in the main beam; therefore, Eq. A-11 simplifies to

$$T_A{}' = \frac{\epsilon T}{L_{GA}} + T_{GA} (1 - \frac{1}{L_{GA}}) + \left[\frac{\Gamma_c}{L_{atm}} + T_{atm} (1 - \frac{1}{L_{atm}}) \right] \frac{1 - \epsilon}{L_{GA}} \quad (A-12)$$

Equation A-12 states that the antenna temperature is determined by assuming that a 100% main beam efficiency antenna is looking at the target and for all practical purposes is sufficiently accurate for high main beam efficiencies.

---

[*] G. J. Gill, Computer Data Corporation, Microwave Products Division, Formerly TRG, Inc., Antenna Model W-858-6.

Antenna temperature $T_A{}'$ represents the temperature at the aperture of the antenna. Antenna insertion (attenuation and mismatch) loss will increase the temperature at the antenna output port (antenna-radiometer interface port) to

$$T_A = \frac{T_A{}'}{L_A} + T_o (1 - 1/L_A) \qquad (A-13)$$

where L_A = antenna insertion loss

T_o = antenna ambient temperature

As an example, the breakdown of the antenna temperature factors, using Eqs. A-11 and A-13, are tabulated for a medium humidity day (w = 17 mm) and an antenna loss L_A = 0.35 dB.

ϵ	Target	Intervening Medium Emission	Sky Temp Reflection	Atm Emission Backlobes	$T_A{}'$	T_A
0	0	11.4	47.8	1.8	61.0	78.8°K
0.25	67.3	11.4	35.8	3.4	117.9	131.3
0.5	134.6	11.4	23.9	5.1	175.0	183.9
0.75	201.9	11.4	11.9	6.8	232.0	236.5
1.0	269.0	11.4	0	8.4	289.0	289.1

From the tabulation it is seen that for a perfectly conducting specularly reflecting target (ϵ = 0), or $\epsilon T = 0$, the antenna temperature is 61°K at the antenna aperture and 78.8°K at the antenna output port. This tabulation illustrates the difficulty of precisely determining the brightness temperature until all the radiometric atmospheric effects are accounted for. In addition, the numerous terrain material properties (dielectric constant, conductivity, surface roughness, surface orientation) and their physical temperatures must be specifically defined to establish the emissivity. Should the physical temperature of the target, and the distribution of water vapor and temperature profile in the atmosphere be measured during the imaging experiments, one

could use Eqs. A-11 or A-12 and A-13 to determine an apparent brightness temperature.

To determine the antenna temperature with the sensor flying directly above the cloud cover, Eqs. A-5 or A-11 are applicable, except that the incident sky temperature term Eq. A-3, must be modified to account for the cloud emission, or

$$T_{sky} = \frac{T_c}{L_{GA}L_{AS}} + \frac{T_{atm_{AS}}}{L_{GA}}(1 - 1/L_{AS}) + T_{GA}(1 - 1/L_{GA}) \quad (A-14)$$

where $T_{atm_{AS}}$ = temperature of atmosphere above the aircraft

T_{GA} = average temperature of cloud and atmosphere from ground to aircraft

L_{AS} = atmospheric loss above the aircraft, Eq. A-9

L_{GA} = atmosphere and cloud loss from ground to aircraft.

REFERENCES FOR APPENDIX A

A-1.   J. Stacey, J. Arnold, "Atmospheric Propagation in the Middle-
Infrared and at 8 - 14 μm", Technology Service Corporation, Final
Report TSC-PD-B408-1, September 28, 1973.   DDC No. AD 915 878.

A-2.   E. Jacobs, J. M. Stacey, "Atmospheric Attenuation Models for
Satellite-to-Earth Links", IEEE Trans. Aerospace and Electronic
Systems, AES-7, 144-149, January 1974.

A-3.   R. C. Hansen, "Low Noise Antennas", The Microwave Jl, pp. 19-24,
June 1959.

A-4.   H. H. Grimm, "Noise Temperature in Passive Circuits", Microwave
Jl, 52-54, February 1960.

A-5.   F. I. Shimabukuro, "Propagation Through the Atmosphere at a Wave-
length of 3.3 mm", IEEE Trans Antennas and Propagation, AP-14,
228-234, March 1966.

A-6.   F. I. Shimabukuro and E. E. Epstein, "Attenuation and Emission
of the Atmosphere at 3.3 mm", IEEE Trans on Antennas and Propaga-
gation, AP-18, 485-490, July 1970.

LABORATORY OPERATIONS

The Laboratory Operations of The Aerospace Corporation is conducting experimental and theoretical investigations necessary for the evaluation and application of scientific advances to new military concepts and systems. Versatility and flexibility have been developed to a high degree by the laboratory personnel in dealing with the many problems encountered in the nation's rapidly developing space and missile systems. Expertise in the latest scientific developments is vital to the accomplishment of tasks related to these problems. The laboratories that contribute to this research are:

Aerophysics Laboratory: Launch and reentry aerodynamics, heat transfer, reentry physics, chemical kinetics, structural mechanics, flight dynamics, atmospheric pollution, and high-power gas lasers.

Chemistry and Physics Laboratory: Atmospheric reactions and atmospheric optics, chemical reactions in polluted atmospheres, chemical reactions of excited species in rocket plumes, chemical thermodynamics, plasma and laser-induced reactions, laser chemistry, propulsion chemistry, space vacuum and radiation effects on materials, lubrication and surface phenomena, photosensitive materials and sensors, high precision laser ranging, and the application of physics and chemistry to problems of law enforcement and biomedicine.

Electronics Research Laboratory: Electromagnetic theory, devices, and propagation phenomena, including plasma electromagnetics; quantum electronics, lasers, and electro-optics; communication sciences, applied electronics, semiconducting, superconducting, and crystal device physics, optical and acoustical imaging; atmospheric pollution; millimeter wave and far-infrared technology.

Materials Sciences Laboratory: Development of new materials; metal matrix composites and new forms of carbon; test and evaluation of graphite and ceramics in reentry; spacecraft materials and electronic components in nuclear weapons environment; application of fracture mechanics to stress corrosion and fatigue-induced fractures in structural metals.

Space Physics Laboratory: Atmospheric and ionospheric physics, radiation from the atmosphere, density and composition of the atmosphere, aurorae and airglow; magnetospheric physics, cosmic rays, generation and propagation of plasma waves in the magnetosphere; solar physics, studies of solar magnetic fields; space astronomy, x-ray astronomy; the effects of nuclear explosions, magnetic storms, and solar activity on the earth's atmosphere, ionosphere, and magnetosphere; the effects of optical, electromagnetic, and particulate radiations in space on space systems.

THE AEROSPACE CORPORATION
El Segundo, California

. . .